ADVANCED FUNCTIONAL MATERIALS
www.afm-journal.de

Selective Laser Sintering 3D Printing of Drug-Loaded Intravitreal Implants

Iria Seoane-Viaño, Carlos Bendicho-Lavilla, Haya Alfassam, Bárbara Blanco-Fernández, Abdul W. Basit,* and Francisco J. Otero-Espinar**

Frequent intravitreal injections are the standard treatment for chronic retinal diseases, but they are costly and inconvenient and carry potential complications. Intravitreal implants have emerged as an alternative approach capable of delivering sustained drug levels over extended periods. However, current implant manufacturing techniques, predominantly extrusion-based, present limitations when processing labile drugs. In this study, biodegradable implants are introduced, fabricated via selective laser sintering (SLS) 3D printing to achieve extended, controlled release of dexamethasone and riboflavin. By adjusting laser scanning speeds, diverse release profiles over 7 months are generated, after which the implant matrix fully degrades in the release medium. SEM-EDX and Raman spectroscopy confirmed uniform drug distribution in the implant, while XRPD, FTIR, and DSC analyses indicated that the drugs remained stable postmanufacturing. Additionally, investigations with ARPE-19 retinal cell cultures demonstrated excellent cytocompatibility of the implant. Overall, the findings confirm that SLS 3D printing is a promising approach for manufacturing intravitreal implants. This technique not only offers compatibility with a wide range of pharmaceutical compounds but also enables the tailoring of drug release by controlling the porosity of the implant. Consequently, SLS-based implants may improve patient outcomes by reducing injection frequency and associated complications.

1. Introduction

Chronic retinal diseases, such as age-related macular degeneration, diabetic macular edema, and diabetic retinopathy, are major contributors to visual impairment globally.[1] These conditions are commonly treated via intravitreal injections of drugs (e.g., anti-VEGF agents and corticosteroids). However, because most of these medications currently lack a controlled-release carrier, patients often face the inconvenience, cost, and potential complications of frequent injections, sometimes every few weeks. Medicated intravitreal implants have been proposed to maintain stable drug levels within the vitreous chamber over extended periods. This approach can significantly improve patient outcomes by reducing the need for repeated injections and lowering treatment-related costs and risks.[2] One such example is Ozurdex (Allergan), which is composed of a poly(lactic-co-glycolic acid) (PLGA) matrix containing 700 µg of

I. Seoane-Viaño, C. Bendicho-Lavilla, F. J. Otero-Espinar
Department of Pharmacology
Pharmacy and Pharmaceutical Technology
Paraquasil Group (GI-2109)
Faculty of Pharmacy
iMATUS and Health Research Institute of Santiago de Compostela (IDIS)
University of Santiago de Compostela (USC)
Santiago de Compostela 15782, Spain
E-mail: i.seoane.viano@usc.es; francisco.otero@usc.es

I. Seoane-Viaño, H. Alfassam, A. W. Basit
Department of Pharmaceutics
UCL School of Pharmacy
University College London
29–39 Brunswick Square, London WC1N 1AX, UK
E-mail: a.basit@ucl.ac.uk

The ORCID identification number(s) for the author(s) of this article can be found under https://doi.org/10.1002/adfm.202508712

DOI: 10.1002/adfm.202508712

H. Alfassam
Advanced Diagnostics and Therapeutics Institute
King Abdulaziz City for Science and Technology (KACST)
Health Sector, Riyadh 11442, Saudi Arabia

B. Blanco-Fernández
Departamento de Farmacología
Farmacia y Tecnología Farmacéutica
I+D Farma Group (GI-1645)
Facultad de Farmacia
iMATUS and Health Research Institute of Santiago de Compostela (IDIS)
Universidade de Santiago de Compostela (USC)
Santiago de Compostela 15782, Spain

A. W. Basit
FabRx Ltd.
Henwood House, Henwood, Ashford TN24 8DH, UK

dexamethasone.[3] Ozurdex is one of the few commercially available injectable and biodegradable treatments currently used to treat certain types of macular edema. Another example, Retisert (Bausch & Lomb), which was withdrawn in 2007, was formulated with a non-biodegradable matrix that ultimately required surgical removal once drug release was complete.[4]

An ideal intravitreal implant should meet three fundamental criteria. First, it must provide sustained drug over extended periods. Second, it must be biocompatible and biodegradable within a reasonable timeframe, eliminating the need for surgical removal. Lastly, the drug and its dose should be tailored to meet the needs of each patient and their specific retinal condition. Poly (D, L lactic-co-glycolic acid) (PLGA) is a biodegradable, biocompatible polymer widely employed in controlled drug delivery. PLGA-based drug delivery systems provide flexible release rates over varying periods, accommodating a diverse range of drugs, from small molecules to biologics.[5,6] Most common techniques for preparing PLGA-based implants involve high-temperature extrusion methods such as hot melt extrusion and fused deposition modeling 3D printing.[7,8] Although effective for many compounds, these high-temperature methods are unsuitable for labile drugs, which can degrade under harsh processing conditions. Consequently, there is a pressing need for alternative fabrication strategies that offer precise control over implant architecture and release profiles while preserving drug integrity.

Selective laser sintering (SLS) 3D printing presents a promising approach to overcoming these limitations. SLS is a 3D printing technique capable of creating 3D structures by sintering powdered materials using a laser beam.[9,10] When using low temperature melting polymers such as PLGA, SLS can operate at reduced temperatures, laser energy, and scanning speeds, thereby making it more suitable for labile compounds.[11–13] Moreover, SLS enables the production of porous structures with controllable pore density and interconnectivity by adjusting parameters such as laser power, scan speed, spot diameter, and chamber temperature, as well as by modifying the characteristics of the powder feedstock.[14,15] This porosity becomes crucial in drug delivery because diffusion through the polymer matrix is the primary mechanism governing drug release; hence, controlling porosity allows for tailoring the release kinetics of the therapeutic agent.[16,17]

The present work focuses on developing biodegradable intravitreal implants engineered to release two model drugs, dexamethasone and riboflavin, over prolonged periods, with complete biodegradation and clearance from the vitreous chamber upon drug release completion. SLS 3D printing has been selected as the manufacturing technology to create these implants with different porosities using Generally Recognized As Safe (GRAS) excipients.[18,19] This strategy uses the technology's capability to design delivery systems that accommodate multiple drugs. By modifying laser speed and implant composition, distinct drug release profiles can be achieved, demonstrating how this manufacturing platform can adapt to diverse clinical scenarios.[9,20] Furthermore, the implants were comprehensively characterized, assessing their morphological properties, physicochemical properties, biocompatibility, and cytotoxicity. Altogether, these findings emphasize the potential of SLS as an innovative manufacturing method for next-generation intravitreal implants.

2. Experimental Section

2.1. Materials

Resomer RG 502 H (PLGA) (Mw: 7–17 kDa; lactide:glycolide = 50:50) was purchased from Evonik (Essen, Germany). Hydroxypropyl cellulose (HPC) grade L (140 000 g mol^{-1}) was obtained from NISSO (Tokyo, Japan). Riboflavin was obtained from Alfa Aesar (Thermo Fisher Scientific, Heysham, UK). Dexamethasone base was purchased from Acofarma (Barcelona, Spain). Hydroxypropyl-β-cyclodextrin (HPβCD) was purchased from Roquette (Lestrem, France). Cell culture reagents (alamarBlue (DAL1025), FBS (Gibco 10270106), Anti-Anti (15240062), F12/DMEM (21331020), and L-glutamine (A2916801) were obtained from Thermo Fisher Scientific (Heysham, UK).

2.2. Methods

2.2.1. Manufacturing of Implants Using Selective Laser Sintering

A total amount of 10 g of PLGA, HPC-L, riboflavin, and dexamethasone was mixed using a mortar and pestle for each formulation (**Table 1**) and sieved through an 850 µm sieve. Afterward, the pharma-ink was transferred to the SLS printer (Sintratec Kit, AG, Brugg, Switzerland). A cylindrical implant template (10 mm length × 2 mm height) was designed using 123D Design (Version 14.2.2, Autodesk Inc., San Rafael, CA, USA). The 3D model was exported as a stereolithography (.stl) file into the 3D printer Sintratec central software (Version 1.1.13, Sintratec, AG, Brugg, Switzerland).

The pharma-ink in the platform reservoir (150 × 13 × 150 mm) of the printer was moved by a sled to a building platform (150 × 13 × 150 mm), creating a flat and homogeneously distributed layer of powder. A surface temperature of 40 °C and a chamber temperature of 28 °C were chosen. The 2.3 W blue diode laser (445 nm) sintered the pharma-ink on the building platform in a pre-defined pattern based on the. stl file. Then, the reservoir platform moved up, the building platform moved down, and the sled distributed a thin layer of powder on top of the previous layer. This process was repeated layer by layer until completion. Implants were removed from the powder bed, and any excess powder was brushed off.

2.2.2. Structure Analysis

The implants' dimensions (diameter and length) were measured using a digital Vernier calliper (GNW Instrumentation, Southport, UK). The mass of each implant was determined using an analytical balance (Sartorius Quintix 35-1S, Gottingen, Germany). The implants' morphological analysis was conducted by observing their external structure through a stereomicroscope with a digital camera (Olympus SZ-CTV/Olympus SC100). The implants' surface topography and internal structure were examined using field emission scanning electron microscopy (FE-SEM) (ZEISS EVO LS15 Scanning Electron Microscope (Thermo Fisher, UK)). All samples were mounted on metal stubs with the aid of carbon. The images were taken at 20 kV.

Table 1. Formulation composition % (w/w) and varying laser scanning speeds (mm/s) employed in the printing of implants.

Implant	Laser speed [mm/s]	PLGA % [w/w]	HPC-L % [w/w]	Dexamethasone % [w/w]	Riboflavin % [w/w]	HPβCD % [w/w]
SLS65	65	65	24	10	1	-
SLS100	100	65	24	10	1	-
SLS100h	100	65	16	10	1	8
SLS100/2	100	65	24.5	10	0.5	-
SLS130	130	65	24	10	1	-
SLS130h	130	65	16	10	1	8
SLS160	160	65	24	10	1	-

2.2.3. Texture Analysis

Texture analysis was performed using a precision Universal Testing Machine AGX-X series (Shimadzu, Kyoto, Japan), equipped with a 50 N load cell and Trapezium X software (Shimadzu, Kyoto, Japan). For this purpose, a blade was secured in the upper support while the implant was positioned on the lower plate. The blade was then gradually lowered at a 1 mm min^{-1} speed until the implant ruptured. The force displacement curve was subsequently recorded from which three key material parameters were derived: breaking strength, failure work, and elasticity.

Breaking strength was determined as the maximum force recorded on the force–displacement curve at the point of material fracture. This was the point at which the implant fails under applied load. Failure work was calculated as the area under the force–displacement curve (AUC) up to the breaking point, representing the energy required to break the material. Elasticity was quantified as Young's modulus, which was the slope of the initial linear portion of the force–displacement curve and reflects the stiffness of the material.

2.2.4. Drug Distribution in the Implant

The distribution of dexamethasone and riboflavin within the implants was analyzed using energy dispersive X-ray analysis (EDX) and Raman spectroscopy. For EDX, a semi-quantitative microanalysis and distribution mapping of the elemental composition of the surface and the core of the implants was conducted using an EDS Ultim Max (Oxford Instruments, Abingdon, United Kingdom) controlled by INCA software (Oxford Instruments, Abingdon, United Kingdom). The acquisition conditions were 20 Kv and a working distance of 8.5 mm for a more precise analysis. Raman spectra were recorded at room temperature on a Raman confocal microscope alpha300 R (WITec, Ulm, Germany) using a 532 nm laser with a power of 7 mW. The implants were sliced and placed in a sampler holder to examine the core of the implant. A total area of 70 × 70 µm was recorded with a lateral resolution of 1 spectrum every 300 µm, for 19600 spectra. Project Five 5.3 (WITec, Ulm, Germany) was used for data processing and imaging.

2.2.5. Crystallinity

The crystal structure and thermal stability of dexamethasone, riboflavin, and excipients, both individually and in their physical mixtures, as well as implants prepared at different laser scanning speeds, were identified and characterized using X-ray powder diffraction (XRD), differential scanning calorimetry (DSC), and thermogravimetric analysis (TGA).

The crystallographic properties of the implants and the powdered formulations were ascertained by a Rigaku MiniFlex 600 X-ray diffractometer (Rigaku, Wilmington, MA, USA) equipped with a Cu X199 ray source ($\lambda = 1.5418$ Å). The intensity of 15 mA and a voltage of 40 kV were applied. Samples were scanned between 2θ angle range 3°–40° with a step size of 0.02° at a speed of 5°/min.

The thermal characteristics of the implants and the physical mixtures were determined using a Q2000 DSC263 instrument (TA Instruments, Waters, LLC, New Castle, DE, USA). The samples underwent a heating process from 0 to 400 °C at a consistent rate of 5 °C per minute in a nitrogen atmosphere with a flow rate of 50.0 mL min^{-1}. Data were collected using TA Advantage software for the Q series (version 2.8.394, TA Instruments, Waters LLC, New Castle, DE, USA) and were subsequently analyzed with TA Instruments Universal Analysis 2000. TA aluminium pans and pin-holed hermetic lids (Tzero) were employed for these measurements, with an average sample size ranging from 3.0 to 5.0 mg.

Thermogravimetric analysis was performed with a Discovery TGA (TA Instruments, Waters, LLC, USA). Samples were heated from 30 to 195 °C at 5 °C min^{-1} in open aluminium pans, and nitrogen was used as a purge gas with a 25 mL min^{-1} flow rate. Data collection and analysis were performed and calculated using TA Instruments Trios software.

2.2.6. Fourier-Transform Infrared Spectroscopy (FTIR)

The infrared spectra of formulations before and after SLS 3D printing were collected using a Spectrum 100 FTIR spectrometer (PerkinElmer, Waltham, MA, USA). All samples were scanned over a range of 4000–650 cm^{-1} at a resolution of 4 cm^{-1} for 6 scans. The spectra of pure dexamethasone drug powder, HPC-L, PLGA, HPβCD, and riboflavin were collected as references.

2.2.7. Near-Infrared (NIR) Spectroscopy and Data Analysis

NIR reflectance spectra were measured using a MicroNIR 1700ES NIR spectrometer (VIAVI, Hertfordshire, UK) equipped with two vacuum tungsten lamps and an InGaAs photodiode

array detector for wavelengths between 950 and 1650 nm (10526–6060 cm^{-1}). Spectra were collected using a probe with a 16 mm diameter collection optic attached to the MicroNIR device. A 99% spectralon reference standard (VIAVI, UK) was used to acquire dark and reference spectra for instrument calibration prior to spectra acquisition.

Four implants of each formulation were analyzed at four different points. The final spectrum for each formulation was obtained by averaging the spectra recorded at the four points on each of the four implants. Data was acquired using VIAVI MicroNIR Pro software (VIAVI, Hertfordshire, UK). Principal component analysis (PCA) was performed on the datasets to visualize the high-dimensional data in low-dimensional space.[21]

2.2.8. Determination of Drug Content

To measure the drug loading of the implants, 3 mg of each implant was dissolved in 10 mL of acetonitrile: phosphate-buffered saline (PBS) (50:50) (% v/v) ($n = 3$). Dexamethasone concentrations were measured using ultra high-performance liquid chromatography (UHPLC) (ACQUITY UPLC H-Class Plus, Waters, Milford, Massachusetts, USA) with an FTN injector and PDA detector. The stationary phase was an ACQUITY UPLC BEH 1.7 µm C18 column, 2.1 × 50 mm (Waters, Massachusetts, USA), and the mobile phase was an isocratic elution of 65% water, 0.1% trifluoroacetic acid (TFA) and 35% methanol pumped at a flow rate of 0.7 mL min^{-1}. The injection volume was 5 µL, and column temperature was set to 35 °C with UV-wavelength of 241 nm. The elution time of dexamethasone base was ≈1.9 min. Chromatograms were processed using Empower three software (Waters, Massachusetts, USA). Subsequently, riboflavin concentrations were measured using a Cary 60 UV–vis spectrophotometer (Agilent, Santa Clara, California, USA) at a UV wavelength of 445 nm.

2.2.9. In Vitro Drug Release

Dexamethasone release patterns were recorded by placing loaded implants (three replicates of each processing condition) in glass vials with 5 mL of PBS at physiological pH (7.4). Vials were kept in an orbital shaker at 37 °C under constant orbital movement (100 rpm). At predetermined times, 0.5 mL aliquots were withdrawn from the medium and replaced with the same volume of fresh medium. Dexamethasone and riboflavin concentrations were measured using the methods described above (2.2.8. Determination of Drug content) and the pH of the samples was measured with a Hanna HI5522 pH meter (Hanna Instruments, Eibar, Spain) at each time point.

2.2.10. Implants Cytocompatibility

Cytocompatibility studies were performed in ARPE-19 cells (CRL-2302, ATCC, American Type Culture Collection, Manassas, VA, USA). Cells were cultured in F-12/DMEM medium supplemented with 10% Fetal Bovine Serum (FBS), 2 mM L-glutamine and 1% of an antibiotic/antimycotic mixture (10000 units mL^{-1} penicillin G, 10 mg mL^{-1} streptomycin and 10 mg mL^{-1} neomycin). The cell culture was maintained at 37 °C, under a 5% CO_2 atmosphere with 95% relative humidity.

To assess ARPE-19 viability in the formulations, the cell metabolic activity was measured by alamarBlue according to manufacturer instructions. ARPE-19 cells (100 µL, 10000 cells/well) were seeded in 96-well plates and incubated overnight. Then, 100 µL of the medium in contact with the implants for 10, 47, 132, and 159 days, were co-incubated with the cells. After 24 h, the cell medium was replaced with 200 µL of alamarBlue 10% in complete cell medium, and cells were again incubated for 1 h. Finally, the fluorescence of the cell media was determined at 544 nm (FLUOstar Omega, BMG LABTECH). The experiments were performed in quadruplicate. Cells cultured in cell media were used as negative controls. The cytocompatibility of each implant component was also assayed separately. PLGA, HPC-L (16%, 24%, and 24.5%), HPβCD (5%, 8%, and 15%), and riboflavin (0.5%, 1%, and 2%) were incubated within PBS, and 100 µL of the medium was co-incubated with the cells.

2.2.11. Statistical Analysis

The NIR raw spectra ($n = 4$) were pre-processed using a Savitzky-Golay filter with a window length of 11 and a polynomial order of 2. Multivariate data analysis was conducted through principal component analysis (PCA). Data pre-processing and multivariate data analysis were conducted using a Python 3.10 script. Statistical analysis of drug release data ($n = 3$) involved a two-way analysis of variance (ANOVA). Tukey's multiple comparisons test was applied to compare the amount of drug released by each formulation over time. For implant cytocompatibility studies ($n = 4$), a one-way ANOVA followed by Tukey's multiple comparisons test was employed to compare the viability of untreated cells against cells exposed to excipients at varying concentrations. Additionally, a two-way ANOVA followed by Dunnett's multiple comparisons test was used to compare the viability of untreated cells with that of cells exposed to the release media of different formulations across multiple time points. All data are expressed as mean ± standard deviation (SD) in figures and tables. Statistical analyses were performed using GraphPad Prism version 8.0 (GraphPad Software, San Diego, CA, USA). A p-value of less than 0.05 was considered statistically significant.

3. Results and Discussion

3.1. Manufacturing of the SLS 3D-Printed Implants

The main objective of this study was to develop biodegradable and biocompatible intravitreal implants capable of the sustained release of two model drugs over an extended period of time. SLS 3D printing was selected as the manufacturing technology due to its ability to create customized structures with varying degrees of porosity and its compatibility with a wide range of biocompatible materials, including celluloses and synthetic biodegradable polymers. Additionally, the short processing time and mild manufacturing conditions make it suitable for various drugs. In this work, dexamethasone was selected as one of the model drugs due

to its widespread use in treating posterior segment eye pathologies. On the other hand, riboflavin, or vitamin B2, was chosen for its antioxidant properties, which, although it is not used as a primary treatment for chronic retinal diseases, might help mitigate oxidative damage in retinal tissues.[22,23]

Due to its high metabolic rate and exposure to light, the retina is highly susceptible to oxidative damage. Oxidative stress has been implicated in the pathogenesis of several retinal diseases, including AMD and diabetic retinopathy.[24,25] Thus, riboflavin might be considered a supportive treatment, particularly in cases where oxidative stress and mitochondrial dysfunction are contributing factors. Although riboflavin already has a well-established therapeutic role in corneal cross-linking procedures to treat keratoconus,[26] it has never been delivered to the intravitreal chamber before. Given the lack of direct studies on riboflavin for intravitreal delivery, a concentration range of 0.5%–1% was selected to minimize the risk of toxicity during local delivery in the eye.

During the SLS 3D printing process, the surface temperature used was 40 °C. Given that PLGA, the main polymer, has a glass transition temperature (Tg) between 40 and 60 °C, it softens during sintering due to the action of the laser. PLGA would act as a binding matrix, encapsulating the other components within it. Moreover, HPC-L, with a Tg between 110 and 130 °C, would likely soften slightly under the application of the laser and partially fuse with the PLGA, contributing to the mechanical properties of the final product by acting as a reinforcing agent within the matrix. Dexamethasone, with a melting point of 262 °C, should remain in a solid crystalline state, physically dispersed within the polymer matrix. Similarly, riboflavin, with a melting point ≈280 °C, should remain a dispersed solid in the formulation. HPβCD, with a Tg between 280 and 300 °C, will likely remain in a solid state and be dispersed within the PLGA matrix, contributing to the drugs' overall stability and solubility enhancement. In view of this, PLGA and HPC-L should support controlled drug release, with the release rate influenced by implant porosity, which can be adjusted by modifying sintering parameters.

Including HPC-L significantly improved the flowability of PLGA during the SLS printing process. HPC-L, with its smooth surface texture and spherical or near-spherical shape, acts as a lubricant by reducing friction, while PLGA, with its irregular particle shapes, is prone to clumping.[9] Additionally, the hydrophilic nature of HPC-L helps to reduce electrostatic charges by absorbing small amounts of moisture from the air, further minimizing powder agglomeration. Most importantly, including HPC-L improved the final implants' dimensional accuracy. PLGA's low thermal conductivity, which limits heat distribution during sintering, negatively impacts the structural integrity of the implants. HPC-L helps mitigate these issues, leading to a better structural integrity of the implants.

In a general context, both laser speed and surface temperature play pivotal roles in determining the total energy of the surface.[15] An increase in surface temperature corresponds to an elevation in the total energy, while an increase in laser speed results in a reduction of the total energy. A higher total energy level is associated with increased degradation, hardness, and object weight.[13] Although laser-induced localized heating by SLS may accelerate the degradation of formulation components, this technology can operate efficiently at lower temperatures and with reduced laser energy and scanning speeds when using a low temperature melting thermoplastic polymer like PLGA. Moreover, including a photo absorbing component has been shown to reduce the degradation of drugs and excipients, as demonstrated in previous studies.[13] Conductive metal particulates, such as carbonyl iron or aluminium, and photo absorbing pharmaceutical-grade colorants, such as Candurin, have been used as photoabsorbing species when pharmaceutical excipients do not efficiently absorb or conduct radiation.[20] However, these photoabsorbing agents may not be suitable and safe for ocular administration, as no studies have investigated their potential intraocular toxicity. In contrast, riboflavin, a natural molecule, could serve as a photoabsorbing excipient while offering antioxidant properties. It can be added in small amounts to the powder blend without posing toxicity risks.[27]

Table 2. Physical properties of the 3D printed implants ($n = 3$).

Implant	Weight ± SD [mg]	Length ± SD [mm]	Diameter ± SD [mm]
SLS65	42.39 ± 2.39	10.93 ± 0.15	3.46 ± 0.22
SLS100	21.65 ± 0.19	10.38 ± 0.04	2.22 ± 0.12
SLS100h	19.04 ± 1.09	10.4 ± 0.2	2.58 ± 0.067
SLS100/2	12.79 ± 3.52	10.08 ± 0.28	1.71 ± 0.45
SLS130	20.10 ± 0.40	10.42 ± 0.219	2.33 ± 0.032
SLS130h	18.39 ± 1.43	10.33 ± 0.21	2.56 ± 0.11
SLS160	14.03 ± 2.06	10.08 ± 0.026	2.01 ± 0.072

3.2. Morphological Characterization of the Implants

Although the theoretical measurements of the cylindrical implants were expected to be 10 mm in length and 2 mm in diameter, slightly different sizes were obtained, showing a correlation between laser speed and implant dimensions (**Table 2**). For example, the implants made with the fastest laser speed of 160 mm s^{-1} (SLS160) had an average length of 10.08 ± 0.026 mm and a diameter of 2.01 ± 0.072 mm, while the implants made with the slowest laser speed of 65 mm s^{-1} (SLS65) had an average length of 10.93 ± 0.15 mm and a diameter of 3.46 ± 0.22 mm. The implants fabricated with intermediate laser speeds showed dimensions between SLS65 and SLS160. This variation in size could be due to the increased interaction time of the laser at lower speeds with the powder bed, leading to excessive energy absorption and melting of the adjacent powder. The prolonged interaction resulted in greater melting of the materials and subsequent infiltration of molten polymer into the gaps between powder particles. As a result, material delamination was reduced, and implant density increased. Moreover, slower scan speeds (e.g., 65 mm s^{-1}) caused greater heat spread, yielding implants with ≈3.5 mm diameter versus ≈2 mm at higher speeds. This oversintering indicates a need to optimize energy input for dimensional accuracy.

This is further confirmed by the higher weights observed in SLS65 implants, which had an average weight of 42.39 ± 2.39 mg. In comparison, SLS100 and SLS130 implants had average weights of 21.65 ± 0.19 mg and 20.10 ± 0.40 mg, respectively, while SLS160 implants had an average weight of 14.03 ± 2.06 mg. Interestingly, SLS100h and SLS130h, although fabricated at the same laser speeds as SLS100 and SLS130, showed slightly lower

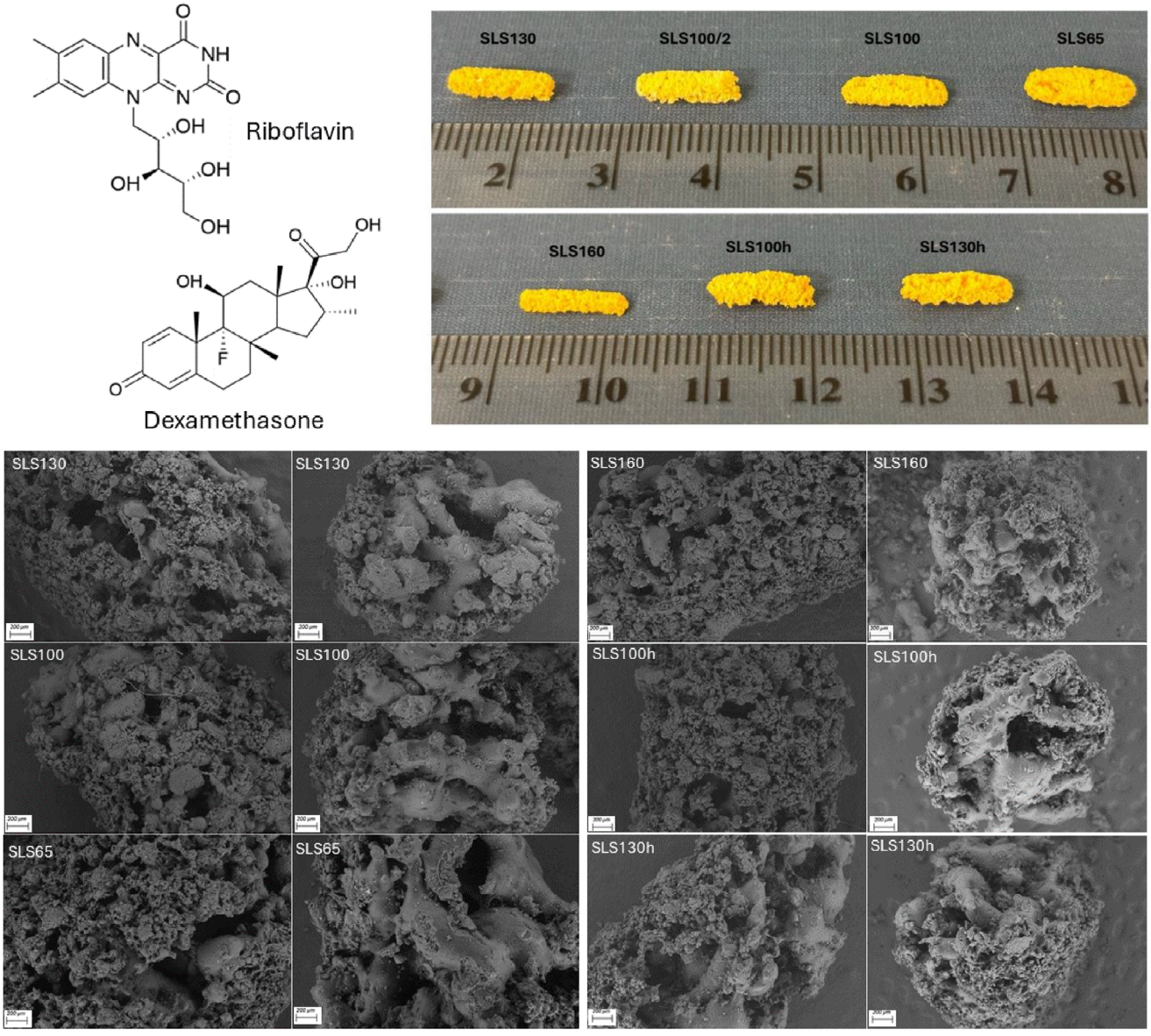

Figure 1. On top, chemical structures of riboflavin and dexamethasone, and representative images of the different SLS 3D-printed implants (scale bar in cm). At the bottom, FE-SEM images of the surface and cross-sections of the implants 3D printed implants.

weights (19.04 ± 1.09 mg for SLS100h and 18.39 ± 1.43 mg for SLS130h). This difference could be attributed to the presence of HPβCD, which does not melt at the temperatures used and remains as solid particles, thereby increasing porosity and reducing density.

A notable case is that of the SLS100/2 implants, which contain only 0.5% riboflavin compared to the 1% included in the other formulations. Although these implants were made at a laser speed of 100 mm s^{-1}, they exhibited an average length of 10.08 ± 0.28 mm and a diameter of 1.71 ± 0.45 mm, with an average weight of 12.79 ± 3.52 mg, making them the smallest in both dimensions and weight among all the formulations. This suggests that riboflavin plays a significant role not only as a therapeutic agent but also in influencing the amount of energy absorbed from the laser due to its yellowish colour. When the concentration of riboflavin is reduced from 1% to 0.5%, it results in smaller and more fragile implants. As a consequence, SLS100/2 implants had to be excluded from the study except for drug release, NIR spectroscopy, and cell culture experiments, as they were too fragile to be handled for other tests. They lacked the adequate handling properties required for therapeutic applications.

FE-SEM images provided information on the surface morphology of the implants fabricated at different laser speeds (**Figure 1**). SLS160 implants exhibited a more porous structure with more defined voids and less compact material, as the reduced energy input from the laser led to less formation of necks between particles. In contrast, SLS65 implants displayed a denser and more compact structure with a significant material melting and infiltration, due to the slower laser speed allowing for greater energy absorption. SLS100 and SLS130 showed an intermediate level of

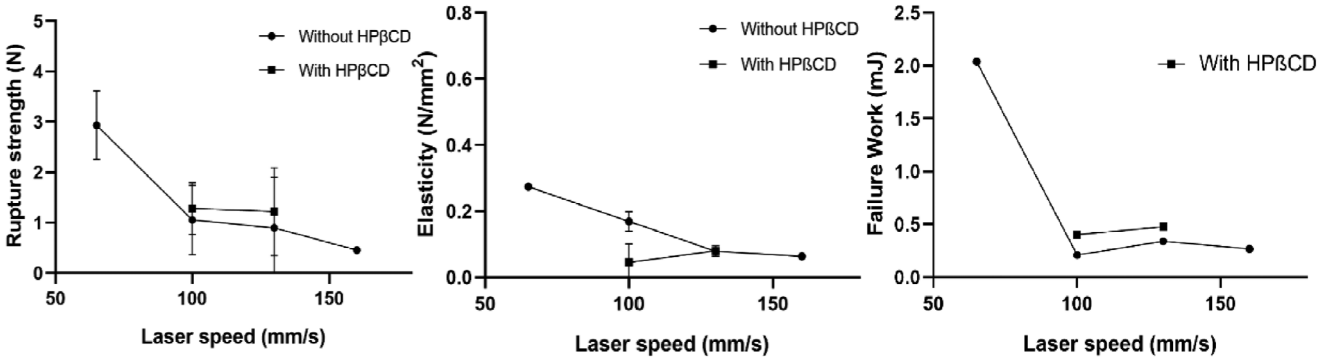

Figure 2. Texture analysis parameters of the implants, including breaking strength, elasticity, and failure work.

porosity and density between SLS160 and SLS65, with surfaces more compact than SLS160 but less dense than SLS65, reflecting the varying degrees of laser interaction time. SLS100h and SLS130h appeared to have slightly different morphologies compared to SLS100 and SLS130. This suggests that the addition of HPβCD may have led to slightly increased porosity or altered surface texture, as indicated by the more granular appearance.

3.3. Mechanical Properties

Texture analysis of the implants revealed a relationship between breaking strength, elasticity, failure work, and the laser speed employed during fabrication (**Figure 2**). The variations observed can be attributed to the laser speed used in the printing process. Notably, implants produced at lower laser speeds, particularly at 65 mm s^{-1}, demonstrated increased mechanical strength. In the case of SLS100h and SLS130h, which included HPβCD in the formulation, the implants showed slightly increased breaking strength and failure work values compared to SLS100 and SLS130. The elasticity values were similar in the case of SLS130h, while SLS100h exhibited slightly lower elasticity. Lower elasticity combined with increased breaking strength and failure work indicates that these implants are stiffer, meaning they could better maintain their shape under stress conditions.

3.4. Drug Distribution in Implants

EDX mapping was employed to localize dexamethasone, the implant's primary drug, within the implant structure. **Figure 3** presents the EDX mapping images of the surface and core of the SLS 3D-printed implants. The drug distribution was identified by detecting the presence of fluorine, which is unique to dexamethasone and absent in the other materials.Table 1 summarizes the elemental distribution for each implant and location.

Overall, the elemental composition is relatively consistent between the core and the surface of each implant. The percentages of carbon, oxygen, and fluorine show only minor differences, indicating uniformity in material distribution from the surface to the core of the implants. This uniformity suggests that the SLS 3D printing process produces implants with consistent material properties throughout the structure, which is important for ensuring reliable performance. The near-uniform distribution of fluorine across both core and surface of the implants suggests a homogeneous incorporation of dexamethasone, supporting a consistent drug release profile throughout the structure.

Raman confocal microscopy images obtained from the surface and longitudinal sections of the implants at higher magnification (**Figure 4**) confirmed the presence of dexamethasone both in the surface and core, as indicated by the elemental analysis. Raman analysis also helped identify riboflavin, which is distributed between the surface and core but appears in lower concentrations and with a more sporadic distribution than dexamethasone.

3.5. Thermal Properties and Crystallinity

TGA analysis was conducted to assess the thermal stability of the different components in the formulations. The TGA curves indicated that all materials remained stable up to ≈300–350 °C (Figure S1, Supporting Information). Since all printing processes were performed below this temperature, none of the components should have undergone thermal degradation.

DSC and XRPD were performed to examine the physical state of the drugs in the formulations. The PLGA curve shows a broad endothermic event ≈50 °C, corresponding to the Tg of the polymer (**Figure 5**). HPC-L and HPβCD exhibited endothermic peaks ≈100–120 °C, likely due to dehydration, but no sharp melting peaks, indicating that both materials are amorphous. Dexamethasone displays a distinct endothermic peak ≈250 °C, indicating its melting point and crystalline nature. Similarly, riboflavin shows a melting endotherm ≈300 °C, confirming its crystalline state.

The melting peaks of dexamethasone and riboflavin were not detected in either the pharma-inks or the implants. However, XRPD analysis (**Figure 6**) indicated the presence of some degree of crystallinity in both the implants and pharma-inks, with bands corresponding to dexamethasone but not riboflavin, which may be below the detection limit of XRPD. If the crystalline fraction is low or the drug crystals are dispersed within an amorphous PLGA matrix, the melting peak may be too broad or weak to be detected by DSC, but XRDP can still detect the crystalline fraction. Another possible explanation could be that, as PLGA melts at lower temperatures, dexamethasone dissolves into the molten polymer and consequently does not produce detectable signals in DSC. Additionally, the presence of dexamethasone in a crystalline state within the implant could be the recrystallisation of the drugs occurring during storage before the assessment

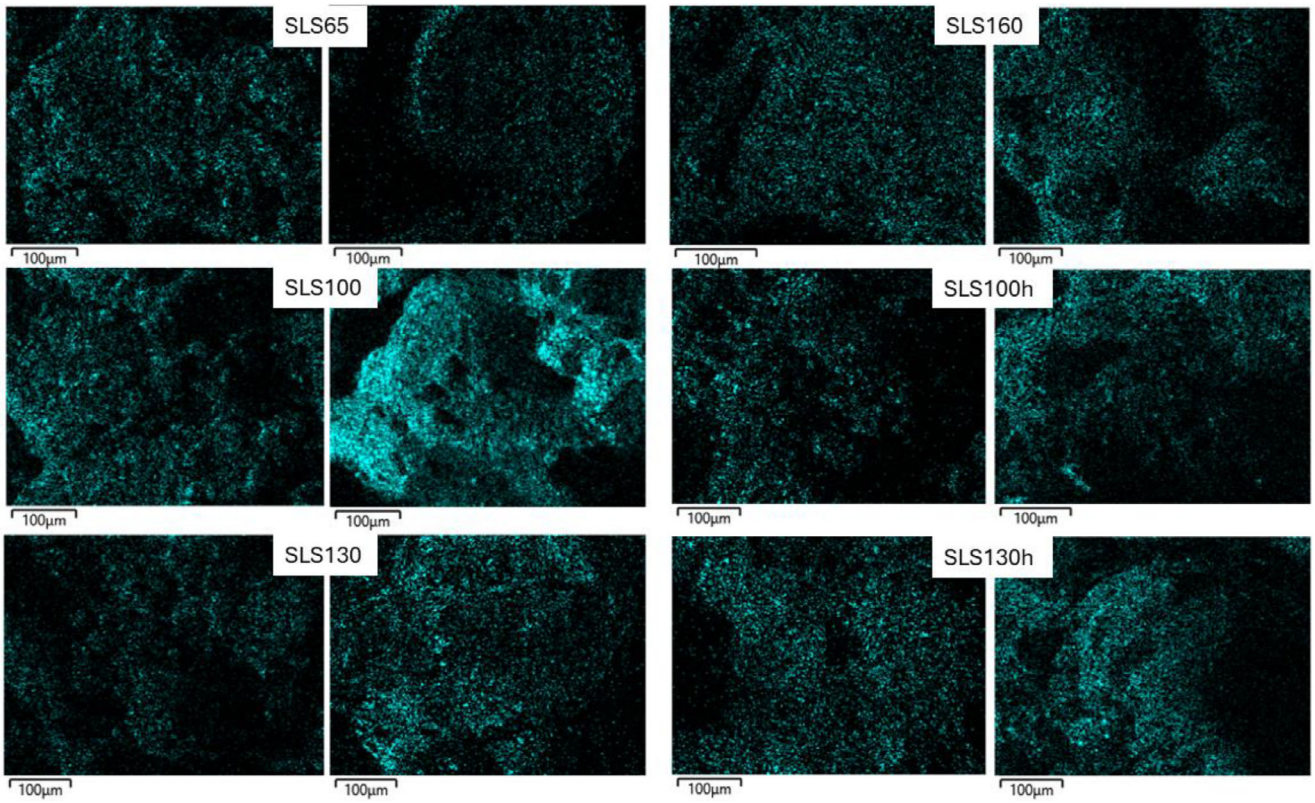

Figure 3. EDX mapping images of the SLS 3D-prited implants. On the left, images of the surface and on the right, images of the core of the implants. The blue dots indicate the distribution of fluorine atoms.

of crystallinity. Upon closer inspection, it can be observed that the bands of SLS65 are broader than those of the other implants. This could indicate more significant disruption of the drug's crystalline structure due to prolonged thermal exposure from the lower laser speed. Consequently, this suggests that the drug may be in a more amorphous form.

FTIR spectroscopy was used to examine the chemical integrity and interactions between the individual components, their physical mixtures (pharma-inks), and the resulting implants produced by SLS 3D printing (**Figure** 7). Varying laser speeds can lead to different levels of heat exposure, potentially causing molecular changes depending on the speed. The FTIR spectrum of PLGA showed characteristic bands ≈1750 cm^{-1} (C═O stretching of ester groups), 1180–1100 cm^{-1} (C-O stretching), and a broad band ≈3000–3500 cm^{-1} (O-H stretching, possibly due to terminal hydroxyl groups). Both HPC-L and HPβCD display broad bands ≈3300 cm^{-1} (O-H stretching), typical for hydroxyl groups, along with bands around 1100 cm^{-1} related to C-O-C stretching in ether groups. Dexamethasone shows distinct bands around 1700 cm^{-1} (C═O stretching), 3400 cm^{-1} (O-H stretching), and 2900 cm^{-1} (C-H stretching). The presence of these bands can be correlated to the functional groups in the dexamethasone molecule (carbonyls, hydroxyls, and aliphatic chains). Riboflavin exhibits characteristic bands around 1600 cm^{-1} (C═N and C═C stretching in aromatic rings), 3400 cm^{-1} (O-H and N-H stretching), 2900 cm^{-1} (C-H stretching), and multiple bands in the 1000–1500 cm^{-1} region, related to aromatic ring vibrations and C-H bending.

The prominent carbonyl groups (C═O) from ketone and ester functionalities of dexamethasone result in a strong band around 1700 cm^{-1}, which is observed in both pharma-inks (with and without HPβCD). This band is also present in SLS100, SLS130 and SLS160, indicating the presence of the drug. As observed in the XRPD spectra, at higher laser speeds, (e.g., SLS160), the material is exposed to the laser for a shorter time, meaning it may not fully melt, potentially leaving the drug in a more crystalline state. In contrast, SLS65, printed at a lower laser speed, only slightly shows the peak in the spectra, suggesting that prolonged exposure to heat could induce a transition from a crystalline to an amorphous state. As no new absorption bands appear in the 1600–1800 cm^{-1}, related to carbonyl group vibrations commonly associated with degradation products or structural changes, the drug is unlikely to have undergone degradation.

Interestingly, neither SLS100h nor SLS130h show the sharp band around 1700 cm^{-1}, which contrasts with the XRPD spectra that indicated sharp band for these two implants containing HPβCD. This discrepancy suggests that while the overall structure remains crystalline, parts of the drug may interact with the cyclodextrin. Dexamethasone's carbonyl group may interact through hydrogen bonding with the hydroxyl groups of HPβCD modifying the vibrational energy levels of the C═O bond. This interaction could result in broader absorption bands in the FTIR spectra, even though the overall crystal structure is preserved, as observed in XRPD. This, in turn, indicates that cyclodextrin affects the drug formulation. The presence of HPβCD may shift or reduce peak intensities if the drug is encapsulated in the

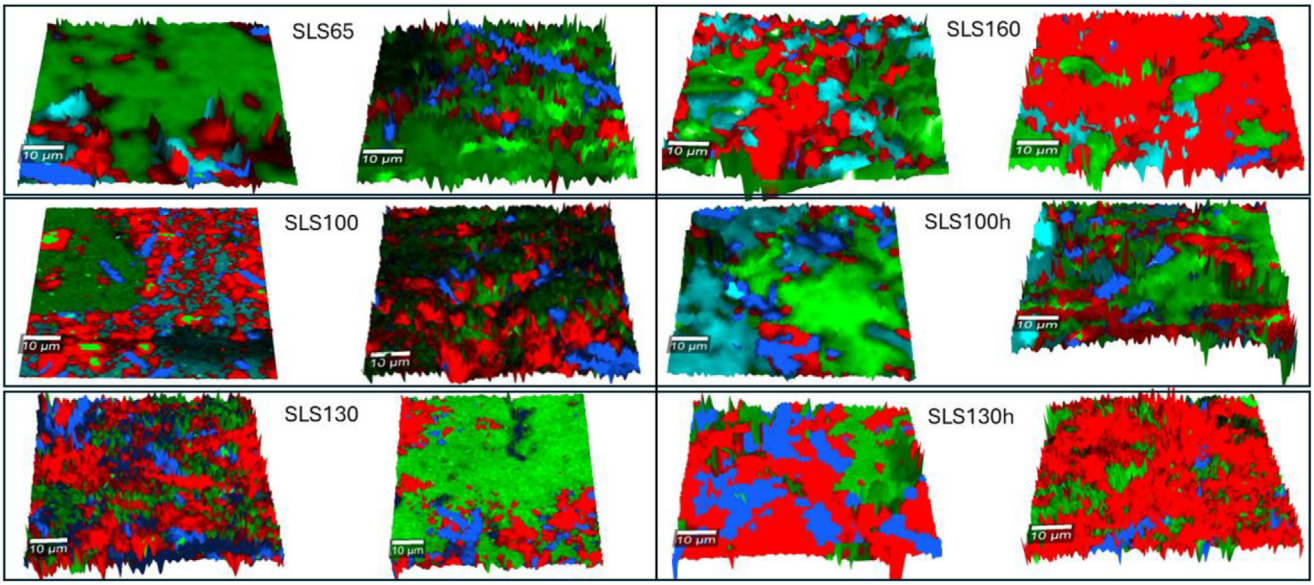

Figure 4. Raman confocal microscopy images show the distribution of dexamethasone (red) and riboflavin (blue) in the surface (left image) and core (right image) of the SLS 3D-printed implants.

cyclodextrin cavity, protecting it from thermal degradation during the SLS printing process.

3.6. NIR Spectroscopy Analysis

NIR spectroscopy can be used to identify variations in laser scanning speed during the SLS manufacturing process, as it can detect subtle changes in the coalescence of particles that form the surface topology of the object. Variations in the NIR diffuse reflectance spectra can be linked to changes in surface scattering from the SLS components, which, in turn, are related to the degree of particle coalescence during the sintering process.[28]

The first-derivative Savitzky-Golay filter was used to enhance and amplify fine details in reflectance raw spectral data, emphasizing inflection points where the reflectance increases or decreases, such as peaks and valleys, while also removing baseline shifts and reducing noise. The first-derivative reflectance spectra revealed two major peak regions where reflectance increased: around 1100–1200 nm and between 1300–1500 nm (**Figure 8**). Differences in peak intensity between the samples were observed in both regions. The implant prepared with the slowest laser speed (SLS65) exhibited larger, more distinct peaks in the derivative spectra, while SLS100h and SLS100/2 show the smallest peaks in the same wavelength regions. The remaining implants exhibited intermediate reflectance, with some spectra overlapping.

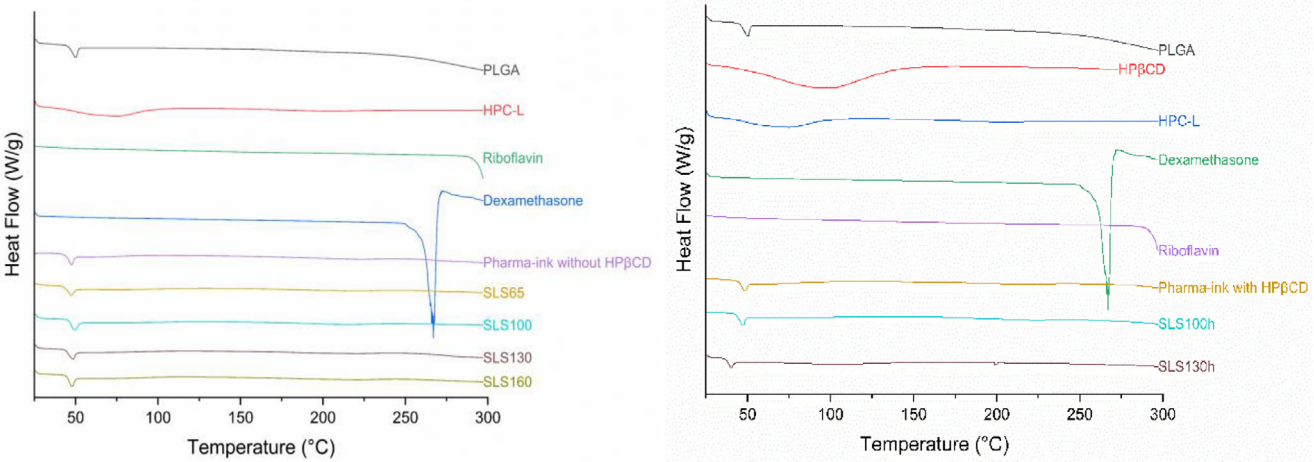

Figure 5. DSC curves of dexamethasone, riboflavin, PLGA, HPCL-L, and HPβCD powders, 3D printed implants, and the physical mixture (pharma-ink) of the excipients and drugs (Exo Up). On the left, pharma-ink and 3D-printed implants without HPβCD, and on the right pharma-ink and 3D-printed implants prepared including HPβCD.

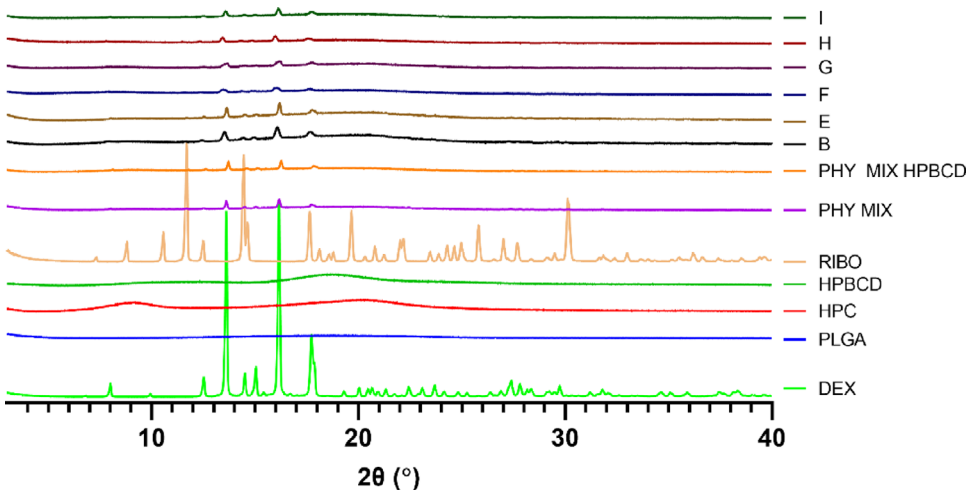

Figure 6. X-ray powder diffractograms of dexamethasone, riboflavin, PLGA, HPCL-L, and HPβCD powders, 3D printed implants, and the physical mixture (pharma-ink) of the excipients and drugs.

This variation can be explained by the differences in particle coalescence achieved at different laser speeds. Slower scan speeds, although not clearly appreciable in the FE-SEM images (Figure 1), promote a smoother surface and more substantial interparticle neck growth, leading to higher reflectance and increased peak intensity. In contrast, faster scan speeds limit particle coalescence, producing a surface more closely resembles the initial powder surface.

SLS100h and SLS100/2 exhibited the least intense peaks. In the case of SLS100h, this may be attributed to the presence of unmelted HPβCD. At the same time, for SLS100/2, the lower peak intensity could result from reduced energy absorption by the laser, possibly due to the less yellowish color caused by the smaller amount of riboflavin in the implants. However, no significant differences were observed among the other implants, suggesting that slight variations in laser speed do not substantially impact reflectance values.

To further investigate how the intensity of infrared light changes when interacting with the surface of the implants, a multivariate analysis was performed to gain insights into the SLS printing process. Standard univariate methods are not applicable in this case, as no isolated spectral bands are specifically linked to scattering effects. Scattering is an optical phenomenon that affects the entire spectral profile rather than appearing as distinct bands.[29] Thus, principal component analysis (PCA), a linear dimensionality reduction technique, was applied to decompose the entire NIR spectrum of each formulation into a single 2D point (Figure S2, Supporting Information). PCA of NIR spectra did not show strong grouping by laser speed, indicating that surface optical properties differ subtly. This analysis confirms that all implants are compositionally similar, with only minor scattering differences at extreme print settings.

3.7. In Vitro Drug Release and Drug Loading

The dexamethasone and riboflavin drug loading of the implants was assessed, with the results displayed in **Table 3**. For dexamethasone, all implants, except for SLS160, exhibited drug loading values slightly above the target. SLS160, however, showed a drug loading below the desired level. In the case of riboflavin, all implants showed drug loading values above the target, likely due to residual, non-sintered riboflavin powder left in the porous cavities.

The release profiles of dexamethasone and riboflavin are shown in **Figure 9A** and **Figure 10**. All the implants showed a controlled release of the drugs during the study time of 210 days, corresponding to almost 7 months. A noticeable decline in the pH levels of the release medium was observed after day 20, with the pH dropping below pH 3. This acidic environment results from the degradation of PLGA, as widely described in the literature. The cleavage of ester bonds generates shorter chain acids, such as glycolic and lactic acids, and the rate at which the acids are generated can exceed the rate of neutralization. Since ester bond hydrolysis is catalyzed by protons, this further accelerates polymer degradation, leading to an increasing drug release rate.[30] This phenomenon can be observed in Figure 9A and Figure 10, where the release rates of both dexamethasone and riboflavin increase from approximately day 20. By day 210, no visible implant remnants remained, indicating essentially complete polymer degradation. While this low pH was evident in the confined in vitro environment, we anticipate the in vivo implications would be significantly mitigated. Under physiological conditions, particularly in vitreous humor, the presence of robust buffering capacity and continuous fluid exchange is expected to mitigate this significant pH drop. Thus, the substantial pH reduction observed in vitro is unlikely to occur to the same extent in vivo.[31] Consequently, it is likely that drug release rates in vivo would be more constant and potentially slower, as the autocatalytic effect from acidic degradation products would be reduced.

Statistically significant differences were observed between the dexamethasone release profiles of the implants on certain days. For instance, on day 3, significant differences were found between SLS65 and all the other implants and between SLS100 and SLS130 compared to SLS100h and SLS130h. On day 20,

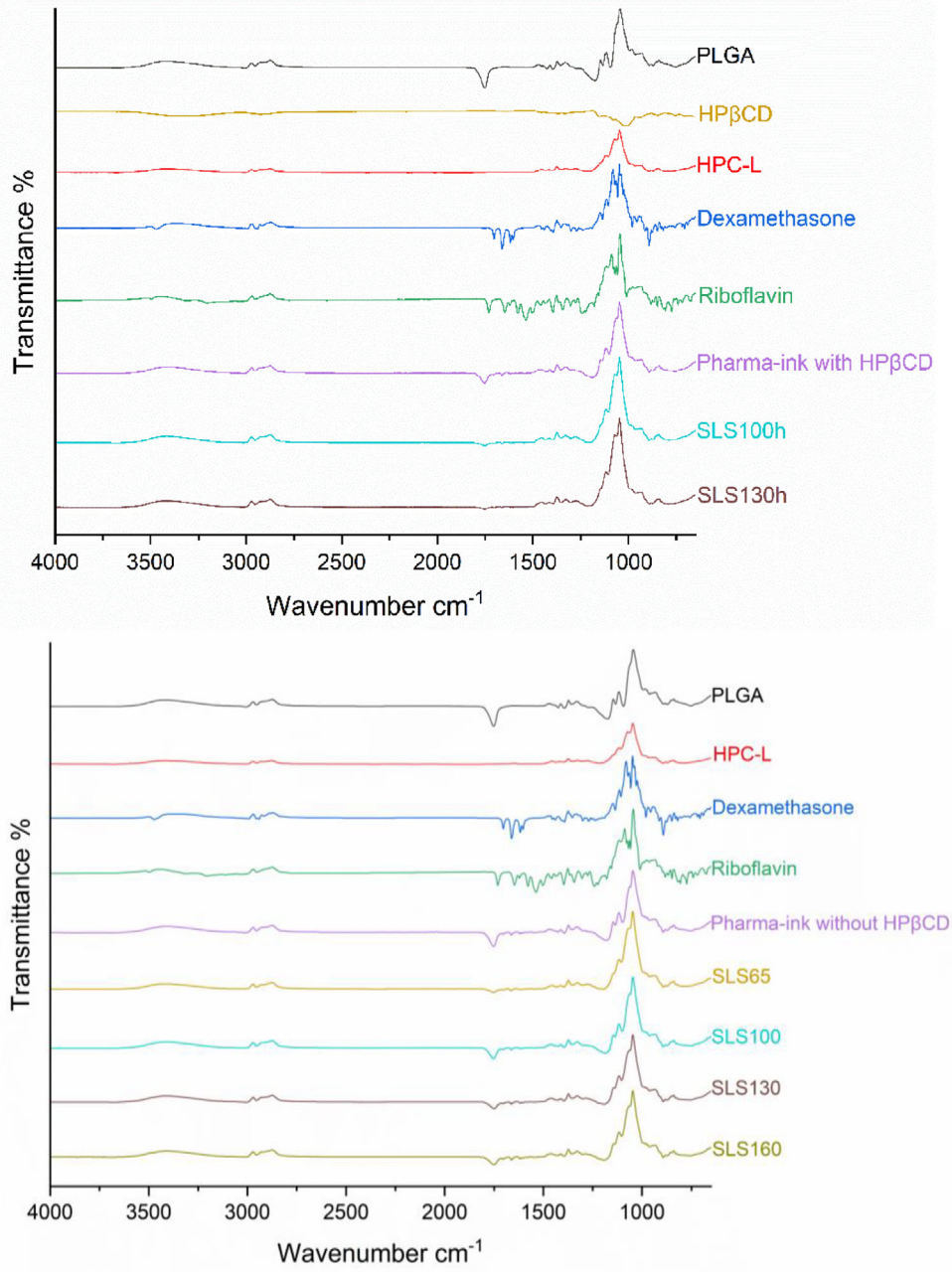

Figure 7. FTIR spectra of dexamethasone, riboflavin, PLGA, HPCL-L, and HPβCD powders, 3D printed implants, and the physical mixture (pharma-ink) of the excipients and drugs. On top, pharma-ink and 3D-printed implants including HPβCD, and bellow pharma-ink and 3D-printed implants prepared without HPβCD.

SLS65 showed significant differences compared to SLS100h, SLS130h, and SLS100/2. By day 75, significant differences were observed between SLS65 and all the other formulations and between SLS100 and SLS130h. Finally, on days 120 and 210, significant differences were found between SLS65 and all the other formulations and between SLS100 and SLS130 compared to SLS130h. Figure 9B shows the linear relationship between laser speed and drug release rate. The slower laser speed resulted in a more densely sintered matrix, leading to significantly slower drug release compared to the higher laser speed. Therefore, higher laser speeds or lower amounts of riboflavin yielded higher release rates, as shown in Figure 9C. This effect is similar to the release kinetics observed in PLGA implants made from low-porosity mesh filaments, where drug release is slower and more controlled due to extended diffusion pathways.[32] Additionally, the filling density of 3D-printed PLGA implants created via extrusion printing also affects drug release. Higher densities lead to fewer interconnected networks or water-filled channels, further slowing drug release.[7] Similarly, PLGA implants prepared using supercritical CO_2 exhibit varying drug release

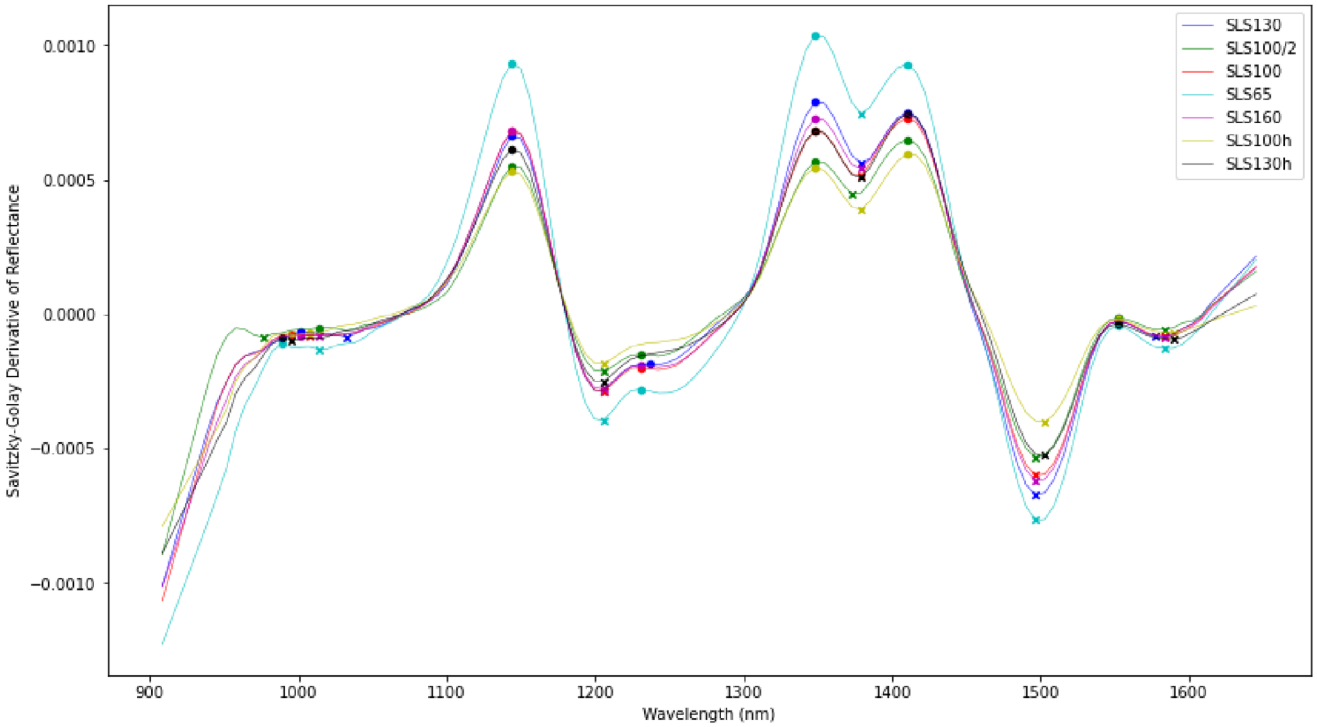

Figure 8. First-derivative Savitzky-Golay near-infrared (NIR) reflectance spectra of the SLS implants manufactured at different laser speeds.

patterns based on different depressurization rates, which affect porosity and can be compared to the present work's laser speed variations.[33]

On the other hand, the differences observed between SLS65, SLS100, and SLS130, and the implants containing HPβCD could be attributed to the presence of the cyclodextrin, which helps solubilizing the drug in the release medium and has a porogenic effect. Due to its high solubility, it dissolves readily, creating pores within the implant. Moreover, SLS100/2 released dexamethasone faster than the otherwise identical SLS100. It is hypothesized that the lower riboflavin content led to a slightly less compact matrix (due to improved laser penetration from the lighter color and reduced solid fraction), thus facilitating diffusion.

In the case of riboflavin, significant differences were also found at the same time points analyzed for dexamethasone, specifically between SLS100/2 and all the other implants. Since riboflavin is a water-soluble molecule, it is expected that implants containing the same amount of riboflavin would exhibit similar release profiles (Figure 10).

After day 150, when the pH begins to rise in the SLS160 and SLS100/2 formulations, a slight decrease in the drug release rate from both implants is observed. This pH increase may be attributed to the faster degradation of these two implants, as they had the lowest weight and mechanical strength, which resulted from the faster laser fabrication speed in SLS160 and the reduced amount of riboflavin used in SLS100/2. As the PLGA/HPC-L matrix degrades and disappears, fewer short-chain acids are produced, allowing the pH of the media to recover.

The cumulative release of dexamethasone reached approximately up to 60% (Figure S3, Supporting Information), which can be primarily explained by the non-sink conditions deliberately chosen for the in vitro setup. The limited volume of the release medium (5 mL) was selected to simulate the confined intravitreal environment, causing the medium to approach saturation and thus slowing further drug release.[34] Although the medium was periodically sampled and replenished with fresh PBS, the small volume still promoted saturation, which in turn may have slowed down the release. This behavior is consistent with in vivo conditions for poorly soluble drugs, where the vitreous humor can also approach saturation as long as solid drug remains in the implant or depot. The vitreous volume inherently creates non-sink conditions, which prolong the release kinetics of corticosteroid implants in vivo.[35] Although not perfect sink conditions, this approach maintained the drug concentration below complete saturation for as long as feasible and better reflects realistic ocular conditions than an infinite sink volume.

Table 3. Drug loading values in the SLS 3D-printed implants.

Implant	Weight ± SD	% Dexamethasone [mean ± SD]	% Riboflavin [mean ± SD]
SLS65	42.39 ± 2.39	101.56 ± 0.52	109.85 ± 0.16
SLS100	21.65 ± 0.19	104.17 ± 0.49	121.11 ± 0.26
SLS100/2	12.79 ± 3.52	103.98 ± 0.32	84.04 ± 0.05
SLS130	20.10 ± 0.40	106.86 ± 0.36	127.53 ± 0.02
SLS160	14.03 ± 2.06	87.68 ± 0.61	124.32 ± 0.14
SLS100h	19.04 ± 1.09	107.40 ± 0.07	113.04 ± 0.03
SLS130h	18.39 ± 1.43	106.76 ± 0.19	117.29 ± 0.11

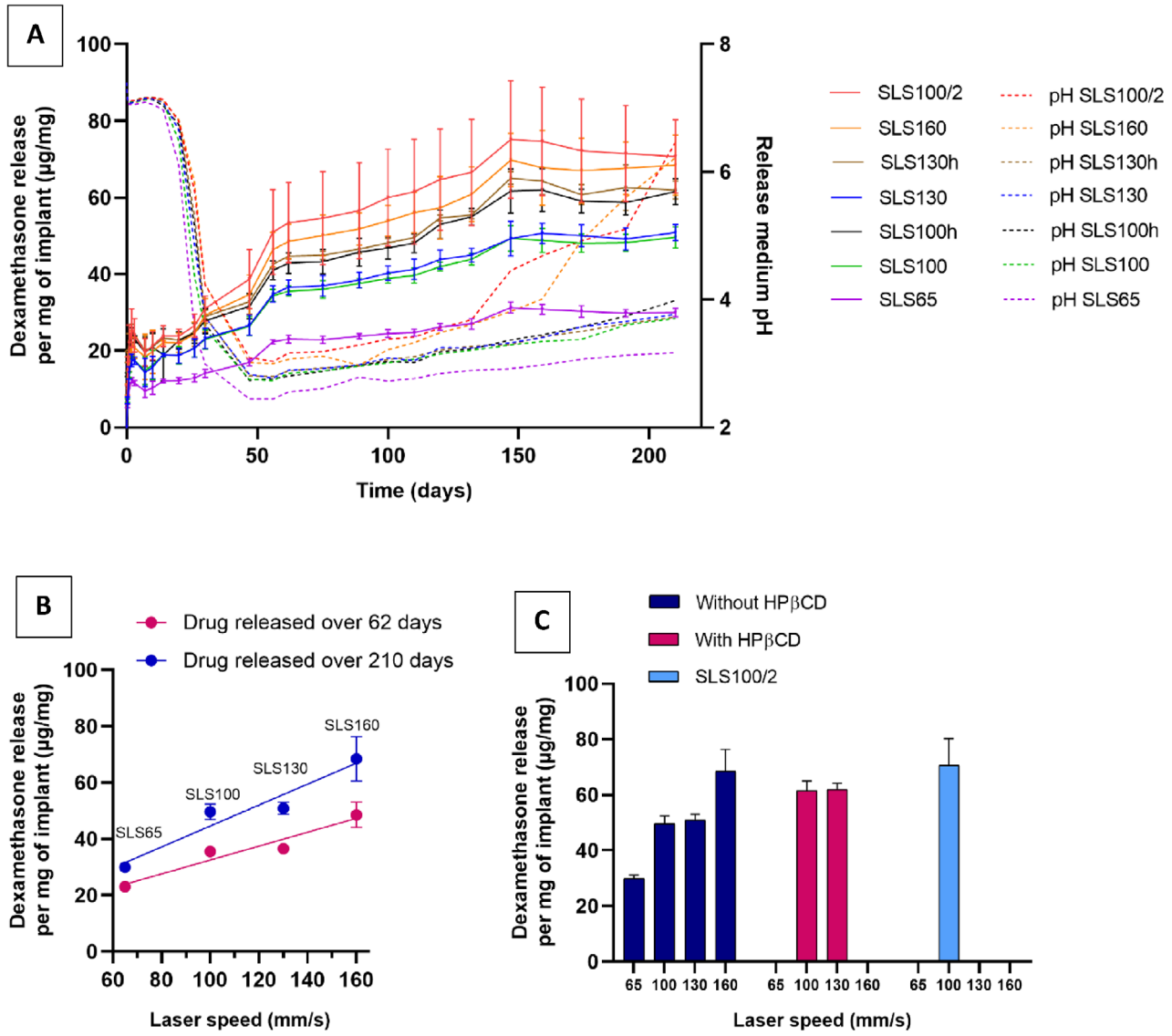

Figure 9. A) In vitro release profiles of dexamethasone from the 3D-printed implants and pH changes during the release in phosphate buffer pH 7.4 ($n = 3$), and detail of the first 7 days of release. B) Linear relationship between laser speed and release rate. C) Relationship between laser speed and amount of riboflavin and release rate.

3.8. Cytocompatibility Studies

The ocular biocompatibility of the implants was assessed by evaluating cytocompatibility in ARPE-19 cells, which closely resemble adult retinal pigment epithelium (RPE) cells in structure and function. The cytocompatibility of all the excipients, HPC-L, HPβCD, and PLGA, was tested at different concentrations. Dexamethasone was excluded from the study, as its cytocompatibility is well-established in clinical use.[33] Riboflavin demonstrated cytocompatibility values above 80% at both the study concentrations and higher levels (up to 2%), supporting its ocular compatibility (Figure S4, Supporting Information). All excipients showed cell viability values close to 100% across the entire concentration range, with no statistically significant differences between untreated cells and those exposed to the excipients. These findings confirm the cytocompatibility of all components used in the implants.

The cytocompatibility of the implants with ARPE-19 cells was further evaluated by incubating cells with release medium collected from the implants at various time points (days 10, 47, 132, and 159). Implants with and without HPβCD were tested (Figure S5, Supporting Information). Exposure to release media from implants fabricated at different laser speeds showed no significant impact on cell viability compared to untreated cells. A slight drop in cell viability was observed at $t = 2$, likely due to a pH decrease from PLGA degradation. However, this is not expected to affect retinal cells in clinical applications, as the buffering capacity of the eye will maintain a stable pH within the intravitreal cavity. Additionally, no statistically significant differences in viability were found between untreated cells

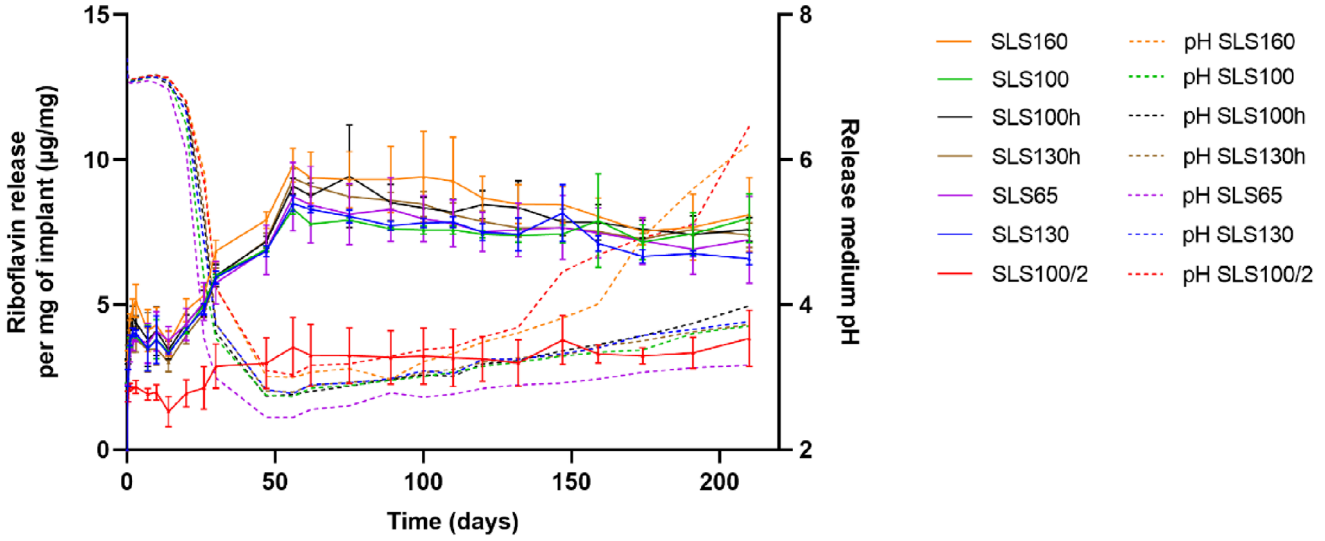

Figure 10. In vitro release profiles of riboflavin from the 3D-printed implants and pH changes during the release in phosphate buffer pH 7.4 ($n = 3$), and detail of the first 7 days of release.

and those exposed to release media samples across various time points.

Overall, the implants developed in this study meet the requirements for an advanced drug delivery device intended for intravitreal administration, capable of sustained drug release over an extended period with complete degradation of the polymer matrix. Different release profiles were achieved by simply adjusting the laser scanning speed, and the technology has proven suitable for the use of widely approved pharmaceutical-grade excipients. Additionally, the solvent-free process makes SLS an attractive option for drugs that are prone to hydrolysis when exposed to solvents. Furthermore, it is possible to recycle or reuse unprinted raw material after the printing process, contributing to greater sustainability and cost-efficiency. Finally, there is room for further optimization of implant dimensions and release patterns, with the ultimate goal of future clinical applications for the treatment of chronic retinal diseases.

4. Conclusion

This is the first study to utilize SLS 3D printing technology to develop intravitreal implants with different release profiles, achieved by varying the laser scanning speeds. The SLS 3D-printed implants effectively controlled drug release over ≈7 months until the matrix completely degraded in the release medium, demonstrating excellent biodegradability. Additionally, the implants exhibited adequate biocompatibility in retinal cell studies. Overall, this study highlights the potential of SLS 3D printing for manufacturing implants with pharmaceutical-grade excipients under mild processing conditions in a fast and cost-efficient process.

Supporting Information

Supporting Information is available from the Wiley Online Library or from the author.

Acknowledgements

This work was partially supported by the Ministry of Science and Innovation of Spain (MICINN) [PID2022-142350OB-C21], Xunta de Galicia [Grupo de Referencia Competitiva, ED431C 2021/26]. I.S.-V. acknowledges Consellería de Cultura, Educación e Universidade for her Postdoctoral Fellowship (Xunta de Galicia, Spain; ED481D-2024-011).

Conflict of Interest

The authors declare no conflict of interest.

Data Availability Statement

The data that support the findings of this study are available from the corresponding author upon reasonable request.

Keywords

3D printing of devices, additive manufacturing of drug products, chronic retinal diseases, intravitreal implants, modified drug release, selective laser sintering 3D printing

Received: April 7, 2025
Revised: July 14, 2025
Published online:

[1] GBD 2019 Blindness and Vision Impairment Collaborators, *Lancet. Global Health* **2021**, *9*, 144.
[2] M. Weber, M. Dominguez, F. Coscas, C. Faure, S. Baillif, L. Kodjikian, S. Y. Cohen, *BMC Ophthalmol.* **2020**, *20*, 206.
[3] S. S. Saincher, C. Gottlieb, *J. Ophth. Inflamm. Infect.* **2020**, *10*, 1.
[4] S. Iyer, A. E. Radwan, A. Hafezi-Moghadam, P. Malyala, M. Amiji, *J. Control. Rel.* **2019**, *296*, 140.

[5] Z. Li, H. Mu, S. W. Larsen, H. Jensen, J. Østergaard, *Int. J. Pharm.* **2021**, *609*, 121183.
[6] C. Bendicho-Lavilla, I. Seoane-Viaño, F. J. Otero-Espinar, A. Luzardo-Álvarez, *Acta Pharm. Sin. B* **2022**, *12*, 621.
[7] C. Bassand, L. Benabed, S. Charlon, J. Verin, J. Freitag, F. Siepmann, J. Soulestin, J. Siepmann, *J. Control. Rel.* **2023**, *353*, 864.
[8] C. Bassand, L. Benabed, J. Verin, F. Danede, L. A. Lefol, J. F. Willart, F. Siepmann, J. Siepmann, *J. Drug Deliv. Sci. Tec.* **2022**, *73*, 103432.
[9] I. Seoane-Viaño, T. Pérez-Ramos, J. Liu, P. Januskaite, E. Guerra-Baamonde, J. González-Ramírez, M. Vázquez-Caruncho, A. W. Basit, A. Goyanes, *J. Control. Rel.* **2023**, *365*, 348.
[10] P. Kulinowski, P. Malczewski, E. Pesta, M. Łaszcz, A. Mendyk, S. Polak, P. Dorożyński, *Addit. Manuf.* **2021**, *38*, 101761.
[11] G. V. Salmoria, P. Klauss, K. Zepon, L. A. Kanis, C. R. M. Roesler, L. F. Vieira, *Virtual Phys. Prototyp.* **2012**, *7*, 107.
[12] K. F. Leong, K. K. Phua, C. K. Chua, Z. H. Du, K. O. Teo, *J. Engineer. Med.* **2001**, *215*, 191.
[13] R. Thakkar, D. A. Davis Jr., R. O. Williams III, M. Maniruzzaman, *Mol. Pharmaceutics* **2021**, *18*, 3894.
[14] G. V. Salmoria, P. Klauss, K. M. Zepon, L. A. Kanis, *Int. J. Adv. Manufactur. Technol.* **2013**, *66*, 1113.
[15] N. A. Charoo, S. F. Barakh Ali, E. M. Mohamed, M. A. Kuttolamadom, T. Ozkan, M. A. Khan, Z. Rahman, *Drug Dev. Ind. Pharm.* **2020**, *46*, 869.
[16] C. Bassand, F. Siepmann, L. Benabed, J. Verin, J. Freitag, S. Charlon, J. Soulestin, J. Siepmann, *J. Control. Rel.* **2023**, *363*, 1.
[17] G. V. Salmoria, P. Klauss, L. A. Kanis, *Lasers Manufactur. Mater. Process.* **2017**, *4*, 108.
[18] A. Awad, F. Fina, A. Goyanes, S. Gaisford, A. W. Basit, *Adv. Drug Delivery Rev.* **2021**, *174*, 406.
[19] Y. Abdalla, M. Ferianc, A. Awad, J. Kim, M. Elbadawi, A. W. Basit, M. Orlu, M. Rodrigues, *Int. J. Pharm.* **2024**, *661*, 124440.
[20] N. L. Funk, P. Januskaite, R. C. R. Beck, A. W. Basit, A. Goyanes, *Int. J. Pharm.* **2024**, *660*, 124299.
[21] I. T. Jolliffe, J. Cadima, *Philos. Trans. R. Soc., A* **2016**, *374*, 20150202.
[22] T. Sinha, L. Ikelle, M. S. Makia, R. Crane, X. Zhao, M. Kakakhel, M. R. Al-Ubaidi, M. I. Naash, *Redox Biol.* **2022**, *54*, 102375.
[23] T. Sinha, M. I. Naash, M. R. Al-Ubaidi, *Front. Cell Developm. Biol.* **2020**, *8*, 861.
[24] Y. Ozawa, *Redox Biol.* **2020**, *37*, 101779.
[25] D. M. van Reyk, M. C. Gillies, M. J. Davies, *Redox Rep.* **2003**, *8*, 187.
[26] A. Conde Penedo, V. Díaz Tomé, A. Fernández Ferreiro, M. González Barcia, F. J. Otero Espinar, *Eur. J. Pharm. Biopharm.* **2021**, *162*, 12.
[27] T. Y. Lee, N. Farah, V. K. Chin, C. W. Lim, P. P. Chong, R. Basir, W. F. Lim, Y. S. Loo, *Nutrit. Res.* **2023**, *119*, 1.
[28] M. A. Beard, O. R. Ghita, K. E. Evans, *J. Appl. Polym. Sci.* **2011**, *121*, 3153.
[29] Y. Abdalla, M. Elbadawi, M. Ji, M. Alkahtani, A. Awad, M. Orlu, S. Gaisford, A. W. Basit, *Int. J. Pharm.* **2023**, *633*, 122628.
[30] C. Bassand, L. Benabed, J. Freitag, J. Verin, F. Siepmann, J. Siepmann, *Int. J. Pharm X* **2022**, *4*, 100131.
[31] R. A. Alshaikh, C. Waeber, K. B. Ryan, *Adv. Drug Delivery Rev.* **2022**, *187*, 114342.
[32] C. Bassand, J. Freitag, L. Benabed, J. Verin, F. Siepmann, J. Siepmann, *Eur. J. Pharm. Biopharm.* **2022**, *177*, 50.
[33] C. Bendicho-Lavilla, I. Seoane-Viaño, V. Santos-Rosales, V. Díaz-Tomé, M. Carracedo-Pérez, A. M. Luzardo-Álvarez, C. A. García-González, F. J. Otero-Espinar, *J. Control. Rel.* **2023**, *362*, 342.
[34] S. Stein, T. Auel, W. Kempin, M. Bogdahn, W. Weitschies, A. Seidlitz, *Eur. J. Pharm. Biopharm.* **2018**, *127*, 270.
[35] S. Awwad, R. M. Day, P. T. Khaw, S. Brocchini, H. M. Fadda, *Int. J. Pharm.* **2017**, *522*, 119.